JOURNAL OF GEOPHYSICAL RESEARCH, VOL. 114, C11010, doi:10.1029/2008JC005216, 2009

Global distribution of the decay timescale of mixed layer inertial motions observed by satellite-tracked drifters

Jong Jin Park,[1] Kuh Kim,[2,3] and Raymond W. Schmitt[1]

Received 29 November 2008; revised 10 August 2009; accepted 18 August 2009; published 5 November 2009.

[1] The decay timescale of mixed layer inertial amplitudes has been estimated from satellite tracked drifter trajectories from 1990 to 2004 as the e-folding timescale of the temporal correlation functions. The decay timescales increase with latitude in all basins except the North Atlantic. A beta dispersion model shows that dephasing leads to meridional variations of the decay timescale in the North Pacific and the Southern Ocean, but meridional variations of the buoyancy structure in the North Atlantic act to compensate the beta effect, leading to a lack of meridional variation of the decay timescale in that ocean.

Citation: Park, J. J., K. Kim, and R. W. Schmitt (2009), Global distribution of the decay timescale of mixed layer inertial motions observed by satellite-tracked drifters, *J. Geophys. Res.*, *114*, C11010, doi:10.1029/2008JC005216.

1. Introduction

[2] The slab ocean model of mixed layer inertial motions as suggested by *Pollard and Millard* [1970] is represented by the following equation:

$$\frac{\partial Z}{\partial t} - fZ = -\frac{\tau}{\rho H} - rZ, \tag{1}$$

where Z is the complex horizontal velocity ($u + iv$) in a mixed layer of depth H and density ρ, τ the wind stress ($\tau_x + i\tau_y$), f the Coriolis frequency, and r a Rayleigh damping coefficient. In many instances, this model has been able to explain observations of inertial motions. Table 1 briefly lists the inertial decay timescales reported in previous studies. A 4 day decay timescale is common. However, longer decay timescales have been observed in high latitudes of the North Pacific. In these previous results, a decay timescale r^{-1} of $2 \sim 20$ days was obtained by fitting the model to moored current meter data to parameterize processes which cause inertial motions to decay in the mixed layer.

[3] Most investigations have focused on the radiation of near-inertial waves (NIW) as the primary process for extracting energy from the mixed layer inertial motion, a process often called inertial pumping [*Price*, 1983]. Horizontal velocity gradients of the wave motion cause convergences and divergences that vertically displace the base of the mixed layer and generate the inertial pumping. Depending on the ocean density structure, the generated internal waves can have a continuous spectrum of vertical wave numbers. NIWs with low vertical wave number propagate downward more quickly [*Gill*, 1984; *Garrett*, 2001; *Furuichi et al.*, 2008]. However, NIWs with high vertical wave number stay for longer times and result in high current shear, thus creating turbulence at the base of the mixed layer [*Eriksen*, 1991; *Hebert and Moum*, 1994]. Strictly speaking, both wave radiation and turbulent dissipation contribute to decay of inertial motions in the mixed layer. According to previous moored measurements, since the waves with long vertical scales carry most of the inertial wave energy [*Gill*, 1984; *D'Asaro et al.*, 1995; *Zervakis and Levine*, 1995], wave propagation plays the dominant role in near-inertial energy decay at the surface, especially when rapid decay occurs [*Balmforth and Young*, 1999].

[4] There have been several theoretical approaches employed to estimate the decay timescale. *Gill* [1984] used a modal decomposition and indicated that interaction among the modes results in decay since each mode rotates at a slightly different frequency. Using the large horizontal length scales of the atmospheric forcing and modal structure, he estimated a near-inertial decay timescale to be longer than a year! Since this timescale is much longer than typically observed, attempts to obtain more realistic values have invoked several mechanisms which contribute to fast propagation of NIWs.

[5] *D'Asaro* [1989] and *D'Asaro et al.* [1995] showed that the beta effect temporally changes the meridional wave number initially imposed by wind forcing $l = l_o - \beta t$ and accelerates decay of the NIWs through the vertical group velocity $Cg_z = -N^2(k^2 + l^2)/(fm^3)$. Together with a realistic forcing scale estimated from the scale and translation speed of midlatitude storms, D'Asaro showed that the beta plane model produces a decay time for near-inertial motions comparable to observations in the northeast Pacific.

[6] *Kunze* [1985] derived a dispersion relation for the near-inertial waves propagating in geostrophic shear flow under the WKB approximation. He pointed out that any term in the dispersion relation, which has a spatial gradient

[1]Department of Physical Oceanography, Woods Hole Oceanographic Institution, Woods Hole, Massachusetts, USA.
[2]School of Earth and Environmental Sciences, College of Natural Sciences, Seoul National University, Seoul, South Korea.
[3]Now at Ocean Science and Technology Institute, Pohang University of Science and Technology, Pohang, South Korea.

0148-0227/09/2008JC005216$09.00

Table 1. Previous Studies That Estimate the Decay Timescales of Mixed Layer Inertial Motions

	Location	Observation Period	Decay Timescale
Pollard and Millard [1970]	(39.1N, 70.2W, 39.1N, 69.6W) North Atlantic	Oct ~ Dec 1968 and Oct ~ Nov 1965	4 days
D'Asaro [1985]	(51N, 136W) North Pacific	Dec ~ Feb 1979	4 days
D'Asaro [1995a, 1995b] and *D'Asaro et al.* [1995]	(47.5N, 140W) North Pacific	Oct 1987	20 days
Shay and Elsberry [1987]	(24N, 94W) North Atlantic	Sep 1988	5 days
Hisaki and Naruke [2003]	(26N, 128E) North Pacific	Aug ~ Sep 1995	4 days
Plueddemann and Farrar [2006]	(25.5N, 29.0W) North Atlantic	Feb ~ Oct 1992	3.7 days
	(27.1N, 69.8W) North Atlantic	Feb–May 1986	3.5 days
	(34.0N, 70.0W) North Atlantic	May–Oct 1982	4.1 days
	(59.5N, 20.8W) North Atlantic	Jun–Sep 1991	1.5 days

can affect the spatial scale of the NIW and thus change its energy propagation speed. *Van Meurs* [1998] listed possible factors determining the decay timescale and especially focused on the effect of spatial gradients in the background vorticity, which changes the horizontal wave number of NIWs similar to beta dephasing. The rectifcation of the horizontal wave numbers can be decribed by an effective beta, $\beta_{eff} = \beta + \nabla_h\zeta/2$.

[7] Previous studies have been mostly concerned with searching for the factors controlling the decay of inertial motions. However, there have been few studies that attempt to integrate the factors affecting the spatial variation of the decay timescale, because appropriate observations and analysis methods to obtain the large-scale variability of the timescales were absent. In this study, we extract the decay timescale from satellite tracked drifter trajectory data and analyze its global scale distribution. In addition, an analytical model of the inertial decay timescale with beta dispersion is applied to the global ocean and compared with observations to understand the dynamics and identify the major factors controlling the distribution of decay timescale.

[8] In section 2, the data and methods for estimating the decay timescale of inertial motions will be introduced. Observations will be described in section 3. Then, a theoretical model is developed in section 4 and compared with the observations in section 5. Limitations of this analysis and its physical interpretation will be discussed in section 6.

2. Data

2.1. Satellite-Tracked Drifter Trajectories

[9] This study on inertial motion decay timescales requires observational data not only with continuous high temporal resolution to trace the evolution of mixed layer inertial motions, but also with a large scale global distribution. The most suitable data set for the analysis is satellite-tracked drifter trajectories, which have both the temporal resolution to resolve inertial motions and global coverage. AOML (Atlantic Oceanographic and Meteorological Laboratory) provided all drifter trajectories whose drogue loss indicators were corrected for inaccurate drogue loss information. Only data that have drogues from 1990 to 2004 are used for the analysis. The occasional bad drifter locations from the data sets have been removed by the quality control method suggested by *Hansen and Poulain* [1996], which is based on the drifter speed between consecutive locations.

[10] Inertial amplitudes are estimated from the drifter trajectories for this study. *Park et al.* [2004] suggested a method to estimate the inertial loops by fitting to short-term trajectories such as the surface trajectory of an Argo float. The size of an inertial loop directly corresponds to the inertial amplitude. The method assumes that the short-term trajectory can be decomposed into a rectilinear motion and an inertial-looping motion. Using a simple weighted fit it estimates the size of the looping motion. In order to use the method, a drifter trajectory is divided into short-term segments to obtain the temporal evolution of inertial amplitudes. All consecutive segments are distinct from each other by about 1 day in terms of the average time in each segment, which allows us to look at inertial amplitude variation with a 1 day resolution. Each segment was required to meet the following criteria: The length of each segment is determined by securing more than 5 fixes that extend longer than 70% of the local inertial period, but cannot be longer than 1.5 days in order to avoid too much overlap with a following segment. The criteria above are based on the error analysis of *Park et al.* [2004] which reports an uncertainty of inertial amplitudes of ~3.4 cm/s for short surface tracks of Argo floats.

[11] This method has a couple of merits. One is that independent inertial amplitude estimates can be obtained even in a single trajectory. Once samples have uncorrelated errors, their correlation functions depend 'not on error statistics' but physical phenomenon. The other merit is that the method can minimize the problems of underestimating amplitudes. Complex demodulation may underestimate the amplitudes [*Park et al.*, 2004] and smooth out the temporal change of the amplitude in the case of rapid damping because of the requirement to compute velocity vectors from consecutive pairs of fixes and the need for trajectory segments several inertial periods in length.

[12] An obvious drawback of the *Park et al.* [2004] method is the possibility of energy leakage from other frequency motions, such as mesoscale eddies and tidal currents even though several data criteria are applied to minimize the uncertainty. Fortunately, the method of estimating temporal correlation functions for the decay timescale may not be significantly contaminated by smaller signal-to-noise ratios where sub- or superinertial currents are stronger (details provided in section 3.4).

[13] Some areas are not considered in this study for various reasons. First, all drifter tracks between 15°S ~ 15°N are removed because the inertial period in the tropics is too long to secure accurate inertial amplitudes from the trajectory segments. The samples near 30° (29°–31°) and higher than 60° are also removed to minimize the energy

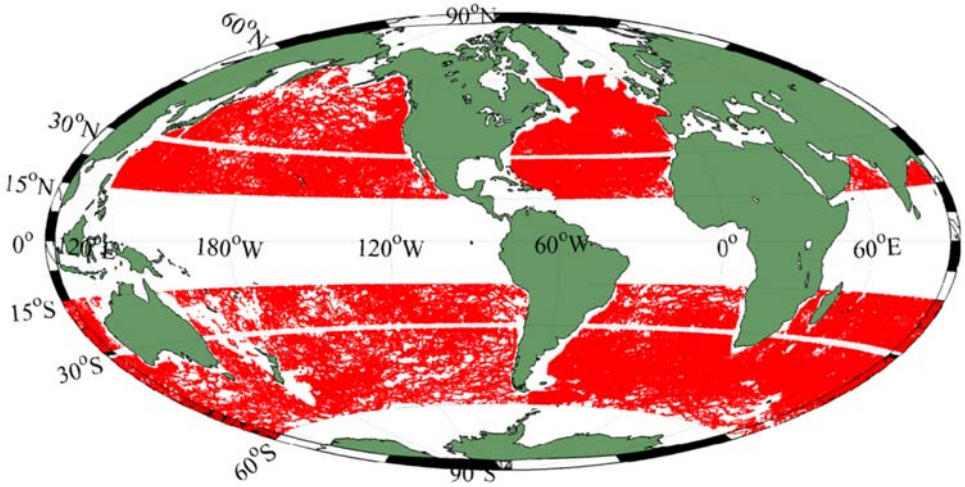

Figure 1. Distribution of inertial amplitude data estimated from satellite tracked drifter trajectories from 1990 to 2004 by using the *Park et al.* [2005] method. The drifters from the bands 15°S ∼ 15°N, 29°N ∼ 31°N, 31°S ∼ 29°S, and latitudes higher than 60°N and 60°S are excluded from the analysis. All data from water depths shallower than 2000 m are also excluded.

leakage from diurnal and semidiurnal tidal currents, although the latitude band has a possibility of NIW generation even at the sea surface by subharmonic resonance from semidiunal tidal motions [*Nagasawa et al.*, 2000; *MacKinnon and Winters*, 2005; *van Haren*, 2007]. Since the samples with a time-independent velocity exceeding 50 cm/s are possibly contaminated by mesoscale eddies or meanders of geostrophic flow, they are excluded from the analysis. Finally, the samples obtained in marginal seas and coastal regions (shallower than 2000 m) which could affect the open ocean statistics are removed. Figure 1 shows the distribution of the inertial amplitude data from the satellite tracked drifter trajectories used in this study. Most of the samples are well distributed in space and are analyzed by ocean basins and latitude bands.

2.2. Other Data

[14] The analytical model used in this paper requires the global distribution of buoyancy structure and wind-forcing scale. The buoyancy structure has been obtained from temperature and salinity profile data from Argo floats for the period 2000 ∼ 2007. The data are available at www.argo.net. The wind-forcing scale has been estimated by using the NCEP-QuikSCAT merged wind product, which has temporal resolution of 6 h and spatial resolution of 0.5° [*Chin et al.*, 1998]. The details of the data treatment are described in section 4.2.

3. Estimation of the Decay Timescale

3.1. Basic Concept

[15] It is believed that most of inertial motions are generated by pulse-like wind forcing such as a storm or a moving front [*Gill*, 1984; *Price*, 1983]. The random timing of the wind forcings that generate inertial motions is presumed to be responsible for the intermittency of inertial motions [*D'Asaro*, 1985]. Also, it is well known that inertial motions are generated within a few hours, and decay within the mixed layer over a few days, much longer than the generation timescale [*Pollard and Millard*, 1970; *Plueddemann and Farrar*, 2006]. Therefore, a time series of inertial amplitudes may be determined by the combination of the random rapid increases and then relatively slow decreases. A typical inertial amplitude time series is shown by *Levine and Zervakis* [1995, Figure 1].

[16] If the pulses of inertial motion in a time series have random timings and are not correlated with each other, the temporal correlations associated with the inertial generation timescale will be negligible in an autocorrelation function. So, only correlations related to the inertial motion decay are retained. Figure 2 shows two different length synthetic time series of inertial amplitude with the prescribed exponential decay pattern of equation 1 and random timings of inertial pulses. The autocorrelation of a short time series (Figure 2a) is very different from the model decay function (Figure 2b). However, the amplitude time series with sufficiently many inertial pulses to assure randomness (Figure 2c) provides an autocorrelation function quite similar to the expected decay function (Figure 2d). Thus, in order to use this approach, we need time series of inertial amplitudes that are longer than a few years to accurately estimate decay timescales. A quantitative requirement for the data length will be given later.

3.2. Use of Drifter Data

[17] In order to estimate the decay timescale of inertial motions, inertial amplitude data obtained from drifters are utilized in this study. A method to estimate scales of motions from Lagrangian measurements was originally developed by *Freeland et al.* [1975]. They searched sample pairs with a preset time window and looked at the correlations of the sample pairs as a function of distance. In this paper, a similar approach is taken but we use a spatial window to estimate temporal correlation. A spatial window is assumed where the inertial amplitudes are highly correlated in space and can be considered as Eulerian samples. The other assumption is of homogeneity in the statistical behaviors of inertial amplitudes; such as uncorrelated errors

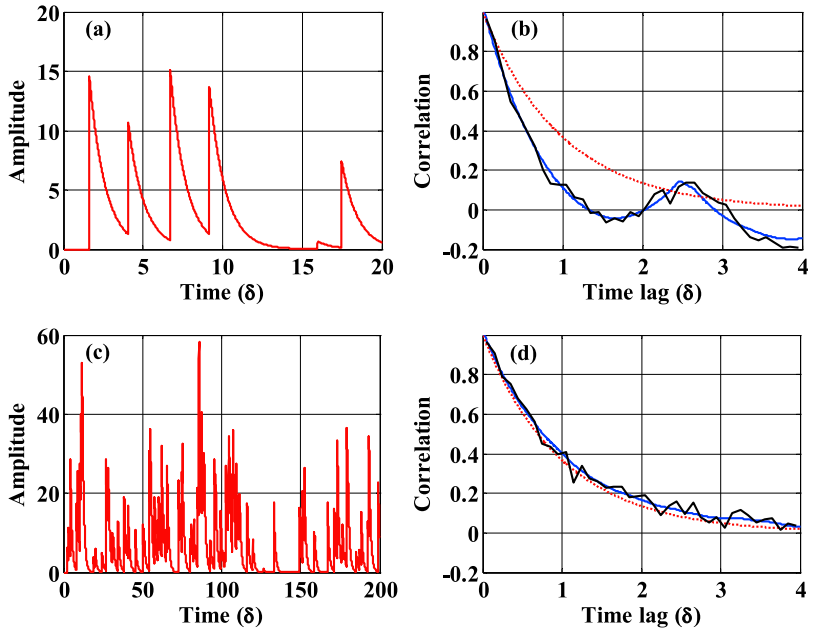

Figure 2. Typical time series of inertial amplitudes generated by using the random storm timing hypothesis [*D'Asaro*, 1985] and a preset decay function, $\exp(-t/\delta)$ with (a and b) the length of 20δ and (c and d) the length of 200δ, where the time is normalized by the preset decay scale δ. Correlation functions in Figures 2b and 2d are obtained from the time series in Figures 2a and 2c, respectively. Blue lines are typical autocorrelation functions. Black lines are temporal correlation functions computed from the random pairs sampling using the method described in section 3.2. Red dotted lines show the preset decay function.

of observation and uniform error variance in a prescribed area.

[18] All inertial amplitudes within a target area are searched to find pairs which meet the above criteria: the distances between any pair must be less than the preset spatial scale. Finally, the pairs with a similar time lag are grouped and used to calculate correlations at various time lags. Figure 3a presents an example of the temporal correlation function within the latitude band of $45 \sim 60°$N of the North Pacific in wintertime. Inertial amplitude pairs within 1 day are highly correlated in Figure 3b, whereas the correlation between pairs is lower for a time lag of 2–3 days in Figure 3c and much lower for 9–10 days lag in Figure 3d. Correlations for most inertial motions after 10 days become smaller than the noise level. Likewise, gathering all correlations according to time lag, we can construct a temporal correlation function (Figure 3a). The correlation function is fitted to an exponential function to get the e-folding timescale. The e-folding timescale is regarded as the decay timescale of the inertial motion in this paper. The exponential decay character of inertial motions is reflected in the pattern of the temporal correlation function (details in Appendix A).

3.3. Spatial Scales of Inertial Motions

[19] In order to determine the temporal scales of inertial motion by computing autocorrelations, the spatial scale must be prescribed so that inertial amplitudes at a certain time are spatially invariant. Similar to estimating the temporal correlation function, the spatial correlations may be obtained by assuming a temporal window. Ideally, the spatial window size becomes the spatial correlation scale of inertial amplitudes obtained at the same time (time lag is zero), but since simultaneous sample pairs are very rare, the tendencies of spatial correlations can be observed by changing the size of the time window.

[20] Figure 4 shows correlation scales obtained from the spatial correlation functions and their dependency on the time window in each ocean basin. Spatial correlation functions (not shown) are fitted to a Gaussian model and their e-folding scales are obtained as spatial correlation scales. The actual spatial scale of inertial amplitudes becomes $\lambda^s/\sqrt{2}$ when the e-folding correlation scale is λ^s, assuming a Gaussian distribution of inertial amplitudes (details in Appendix A). The e-folding scale of the correlation functions becomes larger as the time windows gets smaller because a correlation function with a longer time window than the actual inertial temporal scale violates the assumption of a temporally invariant amplitude within the timescale (Figure 4a).

[21] Figure 4b presents the spatial correlation scales of inertial amplitudes applying the time window of 4 days. Since the radial correlation scales range from $58 \sim 230$ km, corresponding to inertial amplitude scales of $42 \sim 164$ km, it can be assumed that the inertial amplitudes would be uniform within any spatial window less than 40 km. In addition, the smaller spatial window gives better results in the ideal case of unlimited samples. However, as the spatial window gets smaller, the number of samples available to compute the temporal correlation scale also becomes smaller. Therefore, in this paper, the spatial window is set to 40 km in order to secure more than 400 samples at each

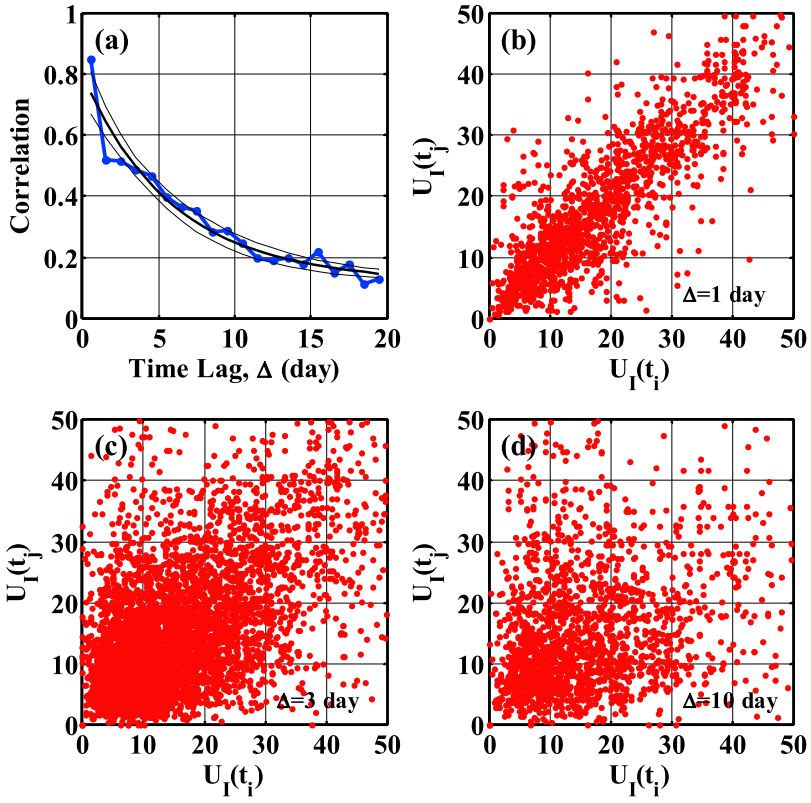

Figure 3. (a) An example of temporal correlation functions (line with circles) of inertial amplitudes within the latitude band of 45 ∼ 60°N in the North Pacific in wintertime. The thick curves are exponential functions fitted to the correlation data. Thin curves show the 95% confidence intervals. Scatterplots of U_i and U_j (b) with less than 1 day lag, (c) with 2–3 days lag, and (d) with 9–10 days lag within 40 km. The pair data sets in Figures 3b ∼ 3d provide correlations of 0.85, 0.52, and 0.29, respectively, which comprise the correlation function in Figure 3a.

time lag (details about the requirements for samples are shown in the next section).

[22] The spatial correlation scale has some geographical variation as shown in Figure 4. These length scales may be determined by the forcing scale, the intrinsic decay timescale, and the background flow field in each ocean basin. The subject of understanding their variability is beyond the scope of this study, though we do address the spatial variability of the decay timescale.

3.4. Error Dependence

[23] Synthetic trajectory data with rectilinear and inertial motion have been used to test the method of estimating the decay timescale. The decay coefficient for the inertial

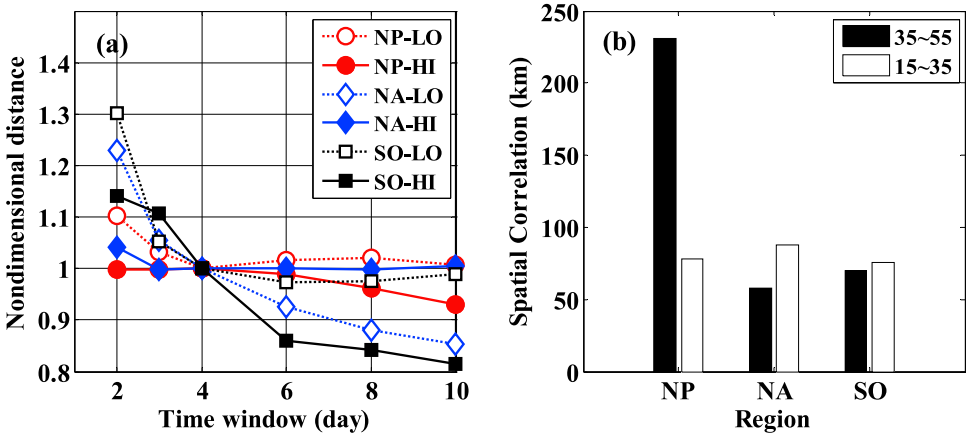

Figure 4. Spatial correlation scale of inertial amplitudes in the North Pacific, the North Atlantic, and the Southern Ocean. (a) Dependence of the correlation scale on the time window. (b) The correlation length scales are normalized by the scales at the 4 day time window. LO and HI denote the zonal bands of 15 ∼ 35° and 35 ∼ 55°, respectively.

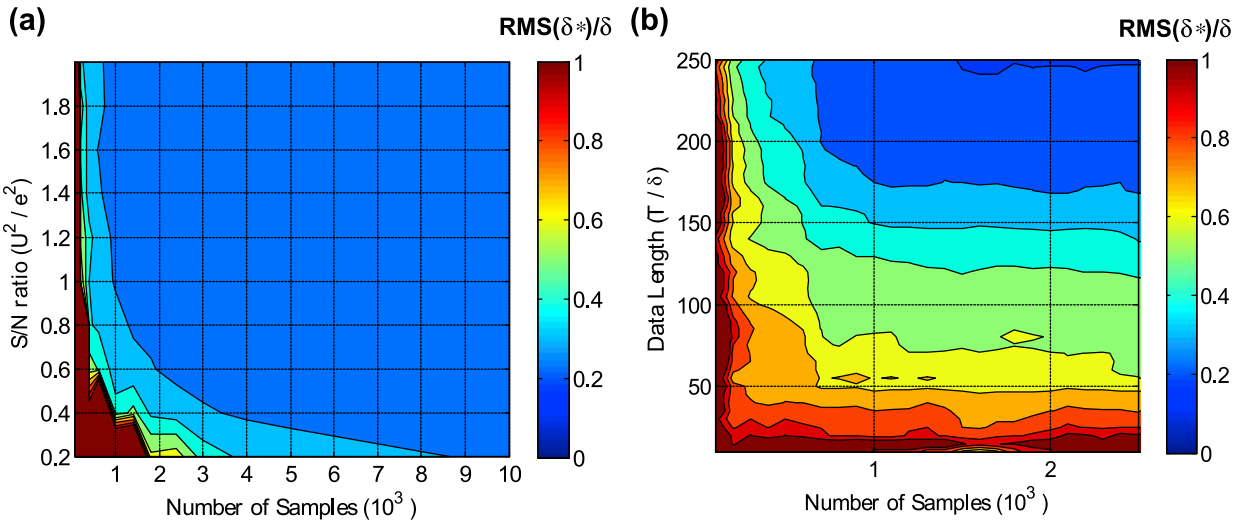

Figure 5. RMS error of the decay timescale predicted by Monte Carlo simulations. Color maps show ratio between RMS error and the preset decay timescale. (a) Dependence of RMS error on the number of samples and the signal-to-noise ratio. (b) Dependence on the number of events.

motion is prescribed as a constant. The magnitudes of rectilinear and inertial motions are randomly selected with ranges of 0 $\sim$ 50 cm/s and position data are sampled at 3 h intervals and with random Gaussian position error of 500 m [*Park et al.*, 2004]. The inertial amplitudes obtained from the method of section 2.1 are used to compute the correlation scale. By changing the factors such as the signal-to-noise ratio, the number of samples, and the number of inertial events, the decay timescales obtained from the estimated correlation function are compared with the preset decay timescale as a true value. These Monte Carlo simulations are repeated 400 times for each experiment and provide the root-mean-squared error (RMS) of the estimates.

[24] Figure 5 shows the dependency of the RMS error on the control factors. Once the number of samples is more than 400, it doesn't contribute to the accuracy of the estimates. Also, the estimation of the decay timescale shows little dependence on the signal-to-noise ratio above a value of 0.6. However, Figure 5b shows that the number of inertial events is the most important factor controlling the accuracy of the decay timescale estimation. With more than 200 events, we can obtain accurate estimates; the RMS error is 20% of the true magnitude. Since the number of tropical storms or disturbances passing by may be 20 $\sim$ 50 in a year [*Visher*, 1925], and the synoptic weather patterns (3 $\sim$ 10 days) may be no more than 100 in a year, in order to secure more than 200 events, the length of the data for estimating the decay timescale should be a few years at least. Since most of moored data and individual drifter trajectory have a duration of less than a year, those data may not be suitable for estimating the decay timescale from traditional autocorrelation functions and Lagrangian timescales. By utilizing multiple drifter trajectories over 15 years, we find that it is possible to estimate the temporal correlation functions and the decay timescales more accurately. The requirement for several years of data limits the extent to which examination of seasonal variations in inertial decay timescale can occur.

3.5. Temporal Correlation Functions

[25] Figure 6 shows some examples of the temporal correlation functions (red lines) that are computed from the inertial amplitude pairs within zonal bands of the North Pacific and North Atlantic. The background shadings present probability density functions (PDFs) of correlation for each time lag estimated by the bootstrap method [*Efron and Gong*, 1983]. Those PDFs exhibit almost Gaussian distributions and the red lines are placed in the middle of the PDFs, which means that each correlation in a temporal correlation function is not severely dominated by large values and is representative of each PDF. Moreover, since the spreads of the PDFs are much smaller than the correlation changes against time lag, each correlation is accurate enough to pick up the temporal correlation function. All correlation functions are fitted to exponential functions and the error of the e-folding timescale has been estimated through the bootstrap method. The correlations are computed for time lags up to 40 days.

[26] A notable feature in Figure 6 is that all the correlation functions have exponential shapes. The functions also exhibit the existence of meridional and basin-wide variations in the decay timescale. The correlations with time lags of less than 4 days have larger values in high latitudes (50°–60°) than in low latitudes (20°–30°) of the North Pacific by about 20% implying that the inertial motions in the North Pacific can survive in the mixed layer at high latitudes for a longer time period. In the North Atlantic, the correlation function at time lags of less than 4 days in high latitudes (50°–60°) is much smaller than that in the high latitudes of the North Pacific. The smaller correlation may result from rapid propagation of NIWs in an ocean environment with deeper high-latitude mixed layer depths (details in section 5). Rapidly propagating NIWs can produce this small correlation at short separation times.

3.6. Meridional Distribution of Decay Timescales

[27] In order to compare the decay timescales from the previous studies listed in Table 1, the North Pacific and

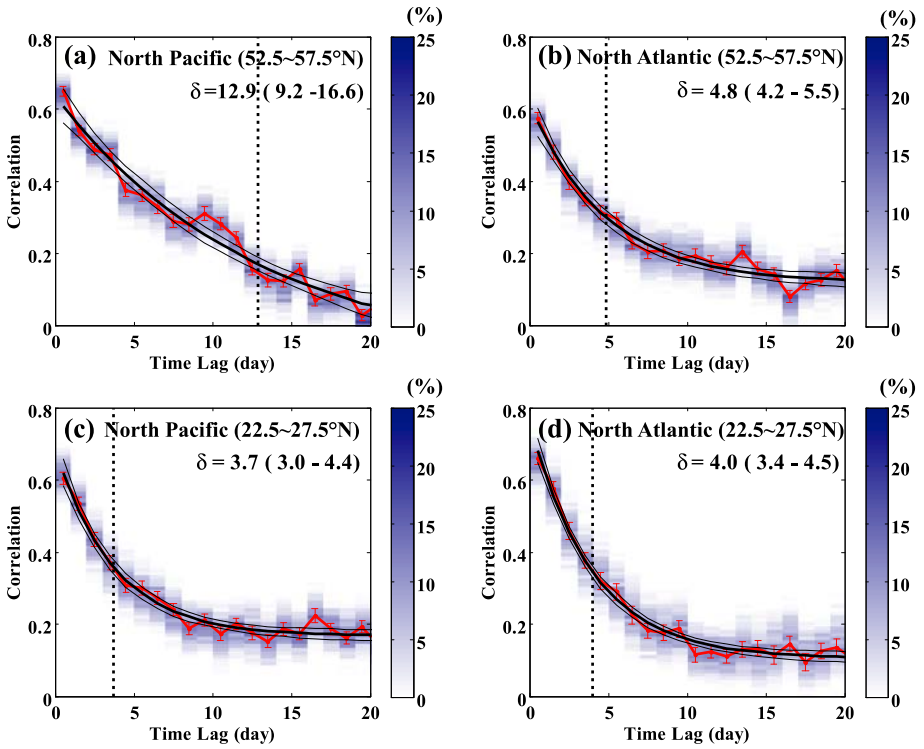

Figure 6. Examples of temporal correlation functions computed from the inertial amplitude data set in the bands (a) 52.5 ∼ 57.5°N and (c) 22.5 ∼ 27.5°N in the North Pacific and (b) 52.5 ∼ 57.5°N and (d) 22.5 ∼ 27.5°N in the North Atlantic. Red lines are the temporal correlation functions and the blue shading shows the histograms obtained from the bootstrap method. Red error bars show the range with 95% of the population. Thick black curves are exponential functions fitted to the temporal correlation functions and thin lines present 95% confidence intervals of the fits.

North Atlantic are divided into three latitudinal regions in summer and winter; low latitude (15 ∼ 30°N), mid latitude (30 ∼ 45°N), and high latitude (45 ∼ 60°N). The temporal correlation functions corresponding to each region and each season are computed by using the inertial amplitude pairs. Figure 7 presents the e-folding times of the correlation functions from drifter observations with bar charts and the decay timescales used in the previous studies with star symbols. Even though the timescales from the previous studies are based on subjective fits to local current measurements with lengths of less than a few months, they are quite consistent with the drifter observations which are basin and climatological average values. Given the amount of data

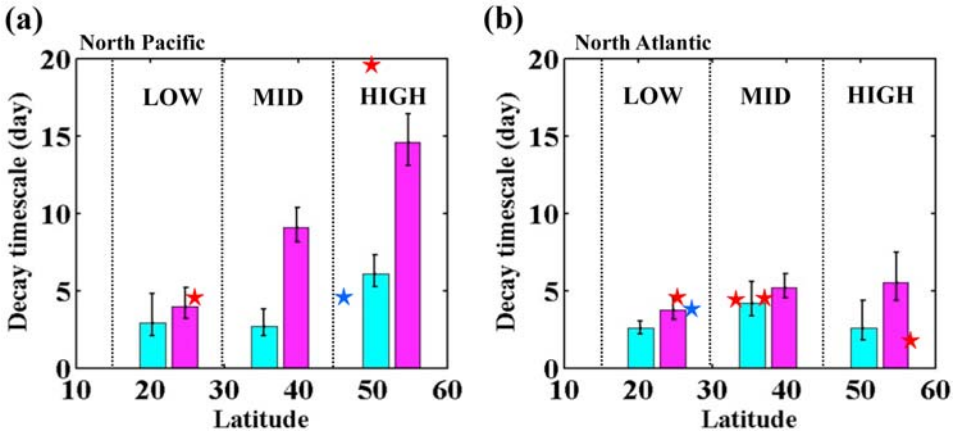

Figure 7. Correlation timescales which are defined as an e-folding time (a) in the North Pacific and (b) in the North Atlantic. Cyan boxes denote winter (December ∼ April) and violet boxes are summer (June ∼ October). The error bars present 95% confidence intervals. Latitude bands are as follows: low are 15 ∼ 30°N, mid are 30 ∼ 45°N, and high are 45 ∼ 60°N. Star symbols denote the decay timescales in Table 1 which are derived from the previous studies (red denotes summer and blue denotes winter).

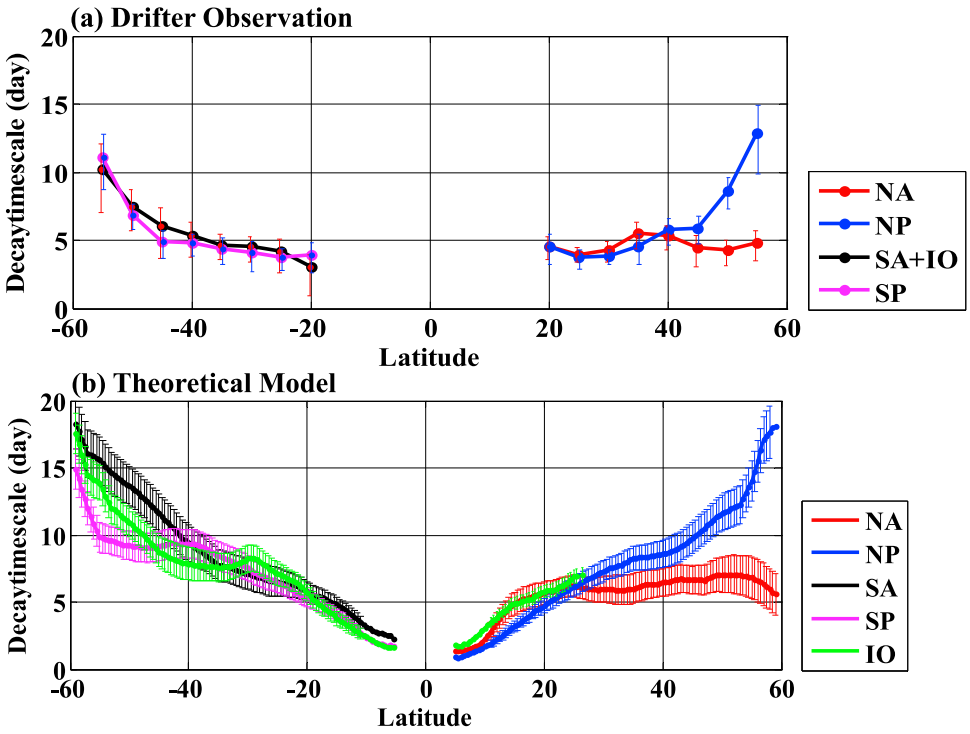

Figure 8. Meridional distribution of the decay timescale estimated from (a) the satellite tracked drifter and (b) the theoretical model results in each ocean basin. Each color corresponds to an ocean basin. Error bars are 95% error ranges estimated by the bootstrap method based on the temporal correlation functions (Figure 8a) and the background data scatter (Figure 8b).

available, no finer temporal resolution than 6 month 'summer' and 'winter' seasons can be achieved at present.

[28] The Ocean Storm Experiment conducted extensive measurements in 1987 and found many new phenomena. *D'Asaro et al.* [1995] pointed out that the inertial decay timescale varied from 2 to 20 days, but was mainly more than 10 days at 50°N in the North Pacific. The interesting thing is, however, that the decay timescales in the whole North Atlantic and the low latitudes of the North Pacific are only around 4 days as shown from 9 moored observations. The basin-averaged drifter observations over 15 years also support the spatial dependency of the decay timescale shown in the previous studies (Table 1).

[29] In an attempt to look at the detailed spatial distribution of the decay timescale in the global ocean, the e-folding timescales have been estimated over 5° zonal bands. The decay timescale seems to vary mainly with latitude by the dependency on f and the beta effect [*D'Asaro*, 1989]. Figure 8a presents the e-folding timescales of temporal correlation functions in each ocean basin. The decay timescales increase with latitude in the North Pacific, South Pacific, Indian and South Atlantic Oceans. The increasing trend is not linear but becomes steeper at higher latitudes, with the longest decay times in the North Pacific. The physical interpretation of this feature will be discussed in sections 5 and 6. The most interesting discovery is that there is no significant latitudinal dependence of the decay timescale in the North Atlantic. Compared with the other ocean basins, the mixed layer inertial motions in the North Atlantic seem to decay more quickly in high latitudes (45 $\sim$ 60°N). Figure 8b is obtained from a theoretical model result which will be revisited and discussed in the next section.

[30] What, then, are the factors controlling the large scale meridional variation of the inertial decay timescale? To address this question, the theoretical approaches of *Young and Ben Jelloul* [1997] and *Moehlis and Smith* [2001] are applied in section 4.

4. Theoretical Model

[31] *Pollard and Millard* [1970] modeled the decay of inertial currents with an arbitrary decay constant in their slab model. Many subsequent works have attempted to determine the detailed mechanisms of this decay. Possible candidates include nonlinear interactions, which transfer energy to other frequencies [*Henyey et al.*, 1986], turbulent dissipation [*Hebert and Moum*, 1994], and downward radiation of NIW excited by inertial pumping into the interior of the ocean [*Gill*, 1984]. Most recent studies have pointed out that the decay timescales given by observations are comparable to the radiation timescale of downward propagation [*van Meurs*, 1998; *Balmforth and Young*, 1999].

4.1. Decay Timescale From Linear Radiation Theory

[32] *Young and Ben Jelloul* [1997] formulate the NIW propagation behavior for interaction with a steady geostrophic flow on a beta plane. Their formulation does not require the vertical normal mode representation as done by *Eriksen* [1980, 1988], *Gill* [1984] and *Zervakis and Levine*

[1995] nor the spatial scale separation assumption, called the WKB approximation [*Kunze*, 1985].

[33] In this paper, we introduce the evolution equation that determines the leading order NIW motion [*Young and Ben Jelloul*, 1997] to address the global distribution of decay timescale shown in the previous sections. The theoretical model in this paper follows the equations derived by *Moehlis and Smith* [2001]. They solved Young and Ben Jelloul's equation by assuming no background flow and a simplified vertical buoyancy structure.

[34] A NIW evolves according to Young and Ben Jelloul's equation

$$\Im A_t + \frac{\partial(\psi, \Im A)}{\partial(x,y)} + \frac{i}{2} f_0 \nabla^2 A + i\left(\beta y + \frac{\zeta}{2}\right)\Im A = 0, \qquad (2)$$

where $\Im$ is a differential operation defined by $\Im A \equiv (f_o^2 N^{-2} A_z)_z$, $\psi(x, y)$ the steady geostrophic stream function, $\zeta = \nabla^2\psi$ the corresponding vorticity, ∇^2 the horizontal Laplacian, $\nabla^2 = (\partial_x^2 + \partial_y^2)$, and the Coriolis frequency f_0. To simplify the analytical model, it is assumed that A and ψ do not vary in the x direction following *Moehlis and Smith* [2001]

$$\Im A_t + \frac{i}{2} f_0 \nabla^2 A + i\beta y \Im A = 0. \qquad (3)$$

[35] In case that the wave scale is O(100 km), which may be a typical forcing scale, βy in the wave refraction term, the 4th term in (2), is larger than $\zeta/2$ by an order of magnitude (not shown). However, there is a rectification effect due to the relative vorticity which may contribute to rapid decay of the NIWs. It will be discussed later.

[36] The buoyancy frequency profile for an infinitely deep ocean is taken to be

$$N^2 = \begin{cases} \varepsilon N_o^2 & for \quad -H_m < z < 0 \\ N_o^2 & for \quad -\infty < z < -H_m \end{cases}, \qquad (4)$$

where $\varepsilon \ll 1$. The objectives of this section are focused not on the detailed vertical propagation structure but the propagation rate out of the mixed layer. Thus, it is reasonable to assume that the buoyancy frequency approaches zero in the mixed layer and is constant below the mixed layer.

[37] Initial conditions for the equation are

$$u + iv = \begin{cases} Ue^{-il_o y} & \text{for} - H_m < z < 0 \\ 0 & \text{for} - \infty < z < -H_m \end{cases}. \qquad (5)$$

The initial inertial motion has a spatial scale imposed by the scale of the wind forcing. Since the zonal scale of wind forcing is usually larger than the meridional scale (up to a factor of two, not shown) and we want to remove zonal variability for simplicity of the equations, only the meridional structure of the initial inertial motion has been considered. Thus, the initial condition to solve the inertial motion equation is taken to be uniform in x; hence A will remain independent of x.

[38] The quantities are nondimensionalized by $y^* = y/Y$, $z^* = 1 + z/H_m$, $t^* = \Omega t$, $N^* = N/N_0$, $(u^*, v^*) = (u, v)/U$, and $A^* = (f_0^2/UH_m^2N_0^2)A$, where H_m is the mixed layer depth and N_0 the buoyancy frequency below the mixed layer. The star superscript denotes nondimensional variables. Nondimensionalizing variables Y and Ω are chosen by considering the balance of the three terms in (3)

$$Y \equiv \left(\frac{H_m^2 N_0^2}{\beta f_0}\right)^{1/3}, \quad \Omega \equiv \left(\frac{\beta^2 H_m^2 N_0^2}{f_0}\right)^{1/3}. \qquad (6)$$

The star superscript is dropped for convenience in the following. With the nondimensionalization, the buoyancy frequency structure is

$$N^2 = \begin{cases} \varepsilon & for \quad 0 < z < 1 \\ 1 & for \quad -\infty < z < 0 \end{cases}. \qquad (7)$$

So the nondimensonalized form of (3) becomes

$$A_{zzt} + \frac{i}{2} N^2 A_{yy} + iy\, A_{zz} = 0. \qquad (8)$$

[39] The boundary condition of zero vertical velocity at the boundary is $A_z = 0$ at $z = -\infty$ and $z = 1$, and the initial condition is $A_{zz} = N^2(u + iv)$ at $t = 0$. By integrating $A_{zz}|_{t=0}$ with respect to z using the boundary condition for A_z, we get the initial condition for A_z as the following:

$$A_z = \begin{cases} \varepsilon(z-1)e^{-il_o y} & for \quad 0 < z < 1 \\ -e^{-il_o y} & for \quad -\infty < z < 0 \end{cases}. \qquad (9)$$

The algebra is quite similar to *Moehlis and Smith* [2001], but we revisit some of the derivations for clarity in Appendix B. Since the solution for the mixed layer NIW is

$$A_{1zz}(y,t) = e^{-iy(t+l_0)} e^{iT^3/3} erfc\left(\frac{1+i}{2\sqrt{3}} T^{3/2}\right), \qquad (10)$$

where the complementary error function (*erfc*) is defined by $erfc(x) \equiv \frac{2}{\sqrt{\pi}}\int_x^\infty e^{-t^2}\, dt$ and $T = ((t + l_o)^3 - l_o^3)^{1/3}$, the temporal evolution of the inertial amplitude in the mixed layer can be expressed as

$$\therefore \alpha_{ML} = \left| erfc\left(\frac{1+i}{2\sqrt{3}} T^{3/2}\right)\right|. \qquad (11)$$

[40] Figure 9 shows the graph of (11) against nondimensional initial wave number l_o. The solution shape is not exactly exponential as the initial wave number goes to zero, but it comes to resemble an exponential at higher wave numbers. That is, the inertial amplitude decays quickly when the inertial wavelength is small. The open circles in Figure 9a present e-folding times of the solution fitted to an exponential function in order to obtain a representative timescale. Negative (positive) initial wave number denotes southward (northward) propagating waves. Northward

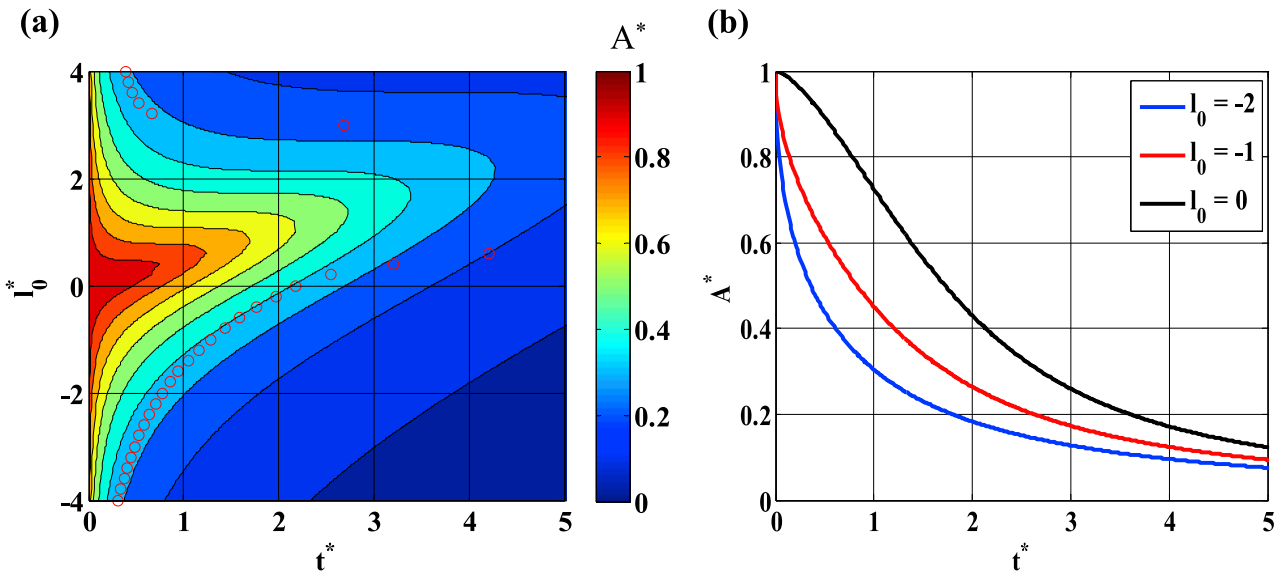

Figure 9. (a) The solution of the dimensionless inertial amplitude evolution against dimensionless time and initial wave number. Red open circles are e-folding timescales of the solution corresponding to the initial wave number. (b) The inertial amplitude time series where the initial wave number is −2 (blue), −1 (red), and 0 (black).

propagating waves experience changing f and their intrinsic frequency gets closer to the local f, where the inertial wave can hardly propagate downward and stays at the surface longer. There is a dramatic transition of inertial amplitude evolution in the positive wave number cases where even a northward inertial wave could propagate downward very quickly and not feel any change of f before getting out of the mixed layer. Further investigation of this effect is beyond the scope of this paper.

[41] The dimensional e-folding time of inertial amplitude evolution becomes

$$\delta'_{\alpha} \equiv \varphi(l_o Y)\left(\frac{f_0}{\beta^2 H_m^2 N_0^2}\right)^{1/3}, \qquad (12)$$

where $\varphi(l_o Y)$ is plotted as the open circles in Figure 9a. When l_o is zero, $\varphi(l_o Y)$ is equal to around 2.3. Figure 9b shows some examples of inertial amplitude evolution according to the initial wave numbers. In the case of infinitely large initial wave (zero wave number), the inertial amplitude decays like a one-sided Gaussian function but, as the wave number becomes higher, it rapidly decreases exponentially. Based on the scale estimation of the wind forcing in the next section, the initial wave number ranges from 0.5 ∼ 2.0 in Figure 9a so most inertial motions are expected to decay exponentially. Detailed discussion on this point will follow in section 6.

4.2. Background Information for the Theoretical Model

4.2.1. Buoyancy Structure

[42] The buoyancy structure and wind scale are necessary to estimate the decay timescale based on the theoretical model of (12). As mentioned in section 2, the large number of profiles obtained from Argo floats provides a global average map of the mixed layer depth (hereafter MLD) and the buoyancy frequency (N) at the base of the mixed layer. In this study, we adapted the optimal definition of MLD using a density-based criterion with $\Delta T = 0.8°C$ suggested by *Kara et al.* [2000]. The buoyancy frequency at the base of the mixed layer is chosen as the maximum value in the buoyancy frequency profile obtained from Argo floats which usually measure temperature and salinity at 5–10 m intervals in the upper thermocline. Figure 10 shows the global distribution of the MLD, N, and the depth (Z_N) where the N is selected, averaged in 2° × 2° bins from 2000 to 2007. The overall features of the MLD and Z_N are very similar and the average difference is around 9 m. The tropical region 10°S ∼ 10°N has larger differences but this is of no consequence for this study. It shows that the MLDs are reasonably well defined. In this model, a vertically uniform buoyancy structure is assumed below the mixed layer.

4.2.2. Initial Wave Scale

[43] As for the initial wave number corresponding to the wind scale, 6 hourly QuikSCAT satellite wind data, high-pass filtered at 72 h, have been used to estimate the wind scale driving mixed layer inertial motions. It is well known that the wind component rotating with the local inertial frequency most effectively generates surface inertial waves [*Price*, 1983]. To determine the wind scales we compute spatial correlations of the winds high-pass filtered in time. Since zonal correlation scales are usually around two times larger than meridional correlation scales, the wave scale change, which controls the vertical group velocity is dominated by the meridional structure. The correlation scale is not very sensitive to the time criteria for high pass filtering if the time is larger than the local inertial period and not larger than the timescale of synoptic wind (less than 10 days).

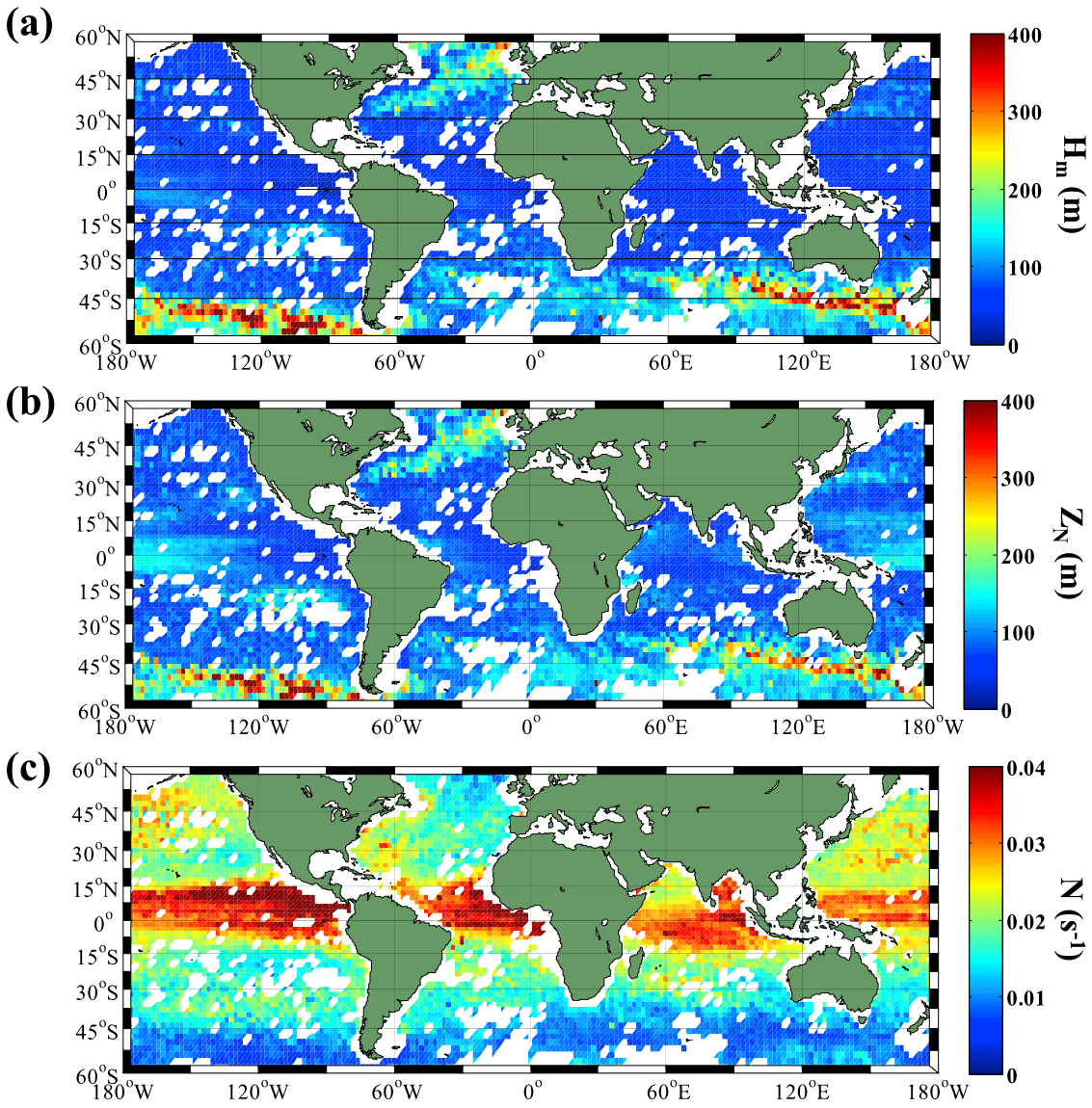

Figure 10. (a) Mixed layer depth defined by *Kara et al.* [2000], (b) thermocline depth defined by maximum buoyancy frequency, and (c) buoyancy frequency in the thermocline estimated from Argo float profile data and averaged in 2° × 2° bins from 2000 to 2007.

[44] In order to check the scale estimated above, the slab ocean model has been run to generate inertial currents and compute the spatial scale of the simulated current. Since the correlation scale from the model result is highly dependent on the damping timescale due to the β effect, we prescribe the damping timescale to be 1 h for these tests. Most of the features and the magnitude of the scale are similar to the results from the band-pass filtered data within 30 km.

[45] Figure 11 presents the meridional scale of the wind associated with inertial motions. The meridional scale distributions of the zonal component and the wind speed resemble each other, which means that a wind with meridional Gaussian shape and the same direction is sufficient to drive inertial currents. However, the red patches in the difference map (Figure 11b) show that the scale of the wind speed is significantly larger than that of the zonal component. In the annual mean sense, these regions are where winds with meridionally opposite signs blow, such as storms that can generate inertial waves of short initial wavelength. The global map of the meridional wind-forcing scale estimated from 2000 to 2007 is presented in Figure 11c. The most striking feature is that the forcing scales increase with latitude up to 50°. Also there are some basin-scale differences at high latitudes (50 ∼ 60°); the scale in the North Atlantic is smaller than in the North Pacific and Southern Ocean by 50 ∼ 100 km. The intrinsic scale and translation speed of storms or fronts may be responsible for this feature.

4.3. Theoretical Model Result

[46] The data of the wind-forcing scale are resampled at the coarser grid of the MLD and N. Assuming that most of the wind generating inertial motions have Gaussian or pulse like shapes in space, the wind correlation scale may be converted to an initial wave number as $l^*_o = l_o Y = 2\pi Y/4\lambda_c$, where λ_c is the meridional correlation scale shown in Figure 11. Since the e-folding scale of the Gaussian function (λ_c) is a half-

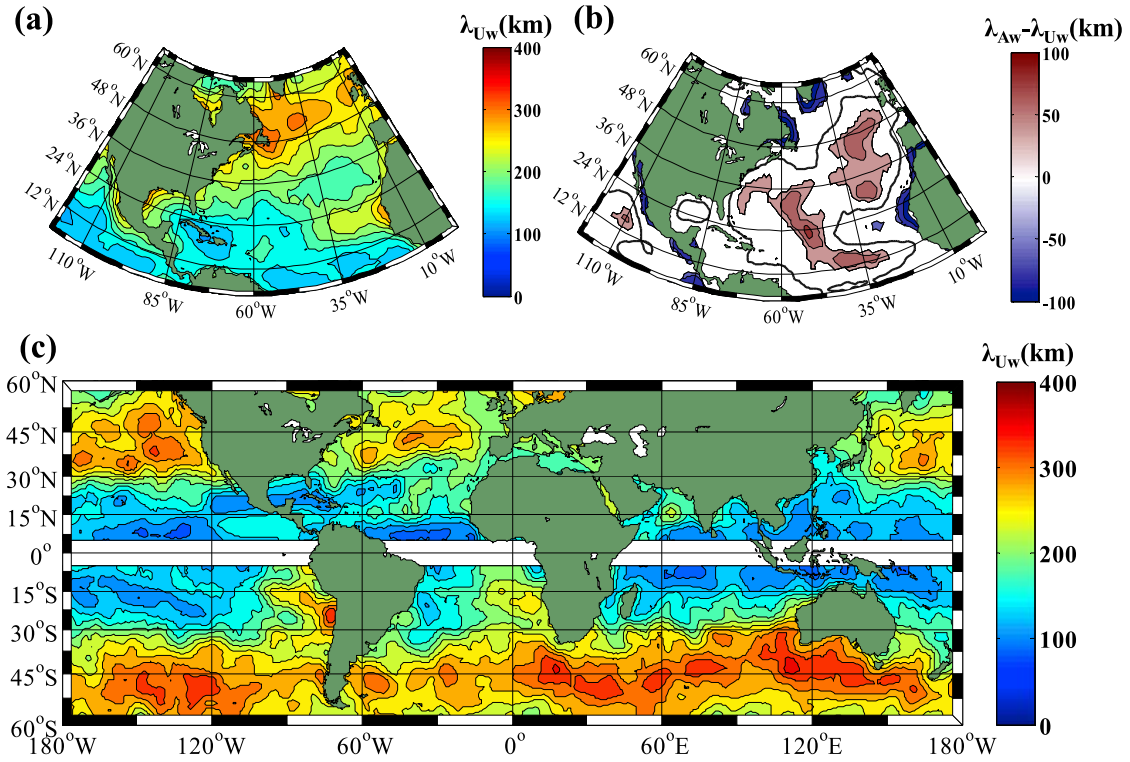

Figure 11. Meridional correlation scales of wind time series in each grid which are obtained from QuikSCAT-NCEP blended product with 6 h and 0.5° × 0.5° resolution and are high-pass filtered with a cut-off of 72 h, implying this is the only part of the wind generating inertial waves. (a) Zonal wind component λ_{Uw} (nearly isotropic) in the North Atlantic in 2000. (b) Difference of the scales between from zonal component (λ_{Uw}) and from wind speed (λ_{Aw}) in the North Atlantic in 2000. The only values above 95% significance level are plotted and the black curve shows zero difference. (c) Zonal wind component from 2000 to 2007.

width of the correlated wind-forcing scale, inertial currents with spatially correlated scale of $2\lambda_c$ must be generated, which corresponds to a wavelength of $4\lambda_c$. Once we get l_o for an individual grid point, φ in (12) is estimated using the solution shape shown in Figure 9b. All information is assembled for (12). The decay timescale from the model is computed in each grid.

[47] Figure 12 presents the global distribution of decay timescale simulated using the theoretical model together with the background information described above. Without any tuning of the model, we get decay timescales in the range of 2 ∼ 20 days comparable to the observations. The most striking features in the map of decay timescale are the characteristic increase with latitude and the differences between the North Pacific and North Atlantic at middle and high latitudes, which are believed to be significant considering the error range (Figure 12b) developed from the background data scatter. Dominant factors controlling the spatial variations of the timescale will be determined in the next section. Additionally, there is a tendency for the timescales in the western part of each ocean basin to be slightly longer than those in the eastern part. Especially, the North Pacific has a clear zonal structure in timescales, with differences at midlatitude (30 ∼ 45°N) of around 3 days. Despite their statistical insignificance, shorter timescales in the western part of the basin are predicted by the model in the North and South Atlantic. This will also be discussed later.

5. Understanding the Model Results

5.1. Comparison of Observations

[48] Figure 8 displays the meridional distributions of decay timescales estimated from the drifter trajectories and computed from the model described in the previous section. As a whole, the meridional and basin-wide variations of the zonal averaged timescales from the model results in Figure 12 are consistent with the observations. The decay timescale simulated by the model also shows increases with latitude in all the ocean basins except the North Atlantic; timescales from 20 to 60°N in the North Atlantic have very different features from the other ocean basins, similar to the observations. The longest decay time is found at high latitudes in the North Pacific.

[49] However, the model results overestimate the observed timescales by around 50% on average. Especially large differences between model and observation appear at midlatitudes (30 ∼ 45°). All basins have almost invariant timescales in 20 ∼ 40° in the observations (Figure 8a), but model results show a linear increase with latitude. Some missing physical processes in the theoretical model may be responsible for this difference such as wave rectification

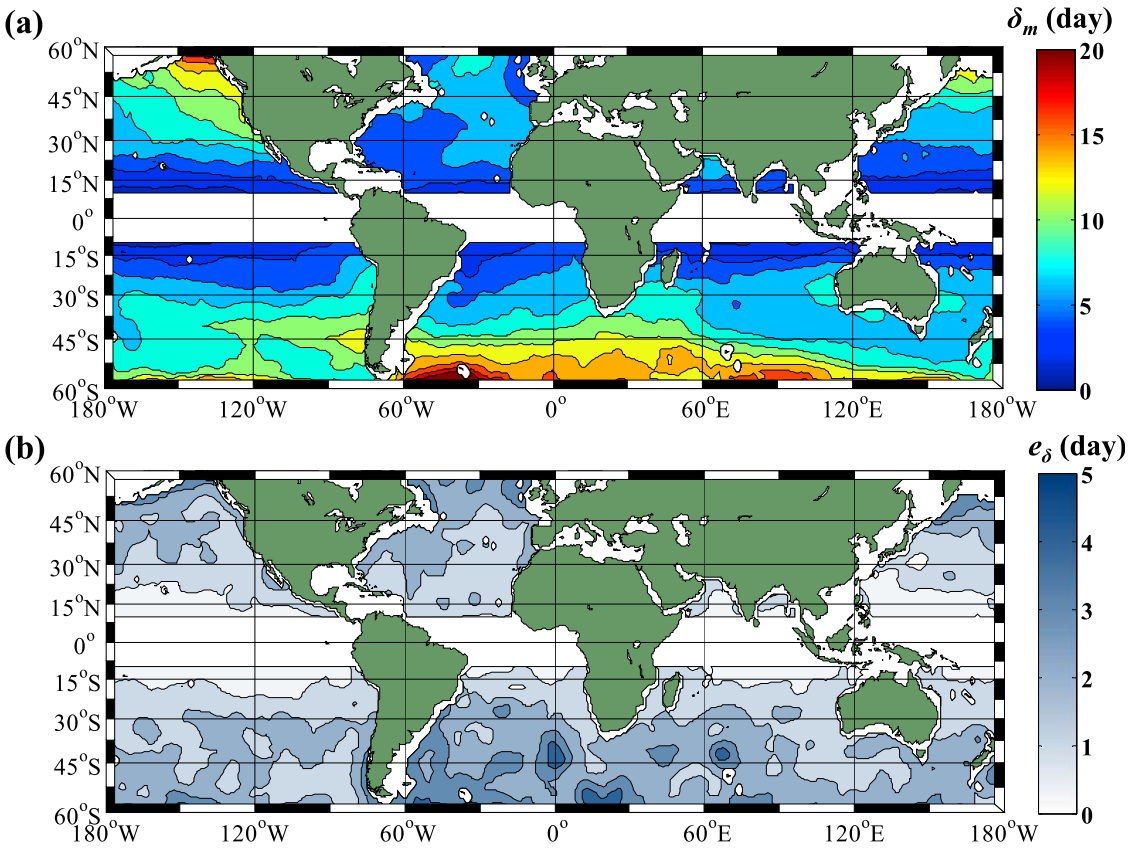

Figure 12. (a) Global distribution of the decay timescale predicted by the theoretical model results. (b) The 95% confidence intervals estimated by the bootstrap method.

effects by background shear flows and turbulent mixing at the base of the mixed layer.

[50] Even though the large error bars in the observation and the model results prevent a detailed comparison, the model mimics the large spatial scale variation of the decay timescale. By decomposing the control factors such as l_0, β, f_o, H_m, and N_o from (12), the dependency of the spatial distribution on each factor can be investigated, which helps us to understand the global distribution of the actual decay timescale.

5.2. Comparison With Each Control Factor

[51] Solution (12) is normalized and taken as log values to separate the factors as follows:

$$\delta_M = \Lambda \cdot \left(\frac{f_0}{\beta^2}\right)^{1/3} \cdot (H_m^2 N_0^2)^{-1/3} \equiv \Lambda \cdot \Gamma^{1/3} \cdot \mathrm{B}^{-1/3} \tag{13}$$

and

$$\begin{aligned}\langle \delta_M \rangle &\equiv \log(\delta_M/\delta_M^c) = \log(\Lambda/\Lambda^c) + \frac{1}{3}\log(\Gamma/\Gamma^c) - \frac{1}{3}\log(\mathrm{B}/\mathrm{B}^c) \\ &\equiv \langle \Lambda \rangle + \langle \Gamma \rangle + \langle \mathrm{B} \rangle,\end{aligned} \tag{14}$$

where the superscript c means basin-averaged value in the North Pacific and δ_M^c is $\delta_M \equiv \Lambda^c \cdot \Gamma^{c\,1/3} \cdot \mathrm{B}^{c-1/3}$. By taking the log of the nondimensionalized factors, the spatial variation of $\langle \delta_M \rangle$ can be expressed as a linear summation of $\langle \Lambda \rangle$, $\langle \Gamma \rangle$, and $\langle \mathrm{B} \rangle$ which represent the forcing-scale effect, beta effect, and stratification effect, respectively. Figure 13 presents how much each factor contributes to the distribution of the simulated decay timescale. If each factor is positive, the factor contributes to make the decay time increase.

[52] The forcing-scale ($\langle \Lambda \rangle$) effects make the decay timescale increase with latitude and slightly larger in the high latitude of the North Pacific, although the forcing-scale effect does not contribute much to basin-wide change of meridional distribution at latitudes higher than 30°. The buoyancy effect ($\langle \mathrm{B} \rangle$) is largely responsible for basin-basin differences of the decay timescale. In the North Atlantic (Figure 13b), the meridional variation of the buoyancy effect term seems to compensate for the beta effect. Thus, the decay timescale in the North Atlantic hardly varies with latitude between 20°N and 60°N because of the unique meridional structure of the stratification. Also the positive effect of the buoyancy term around 50°N in the North Pacific (Figure 13a) makes the decay timescale larger than in the South Pacific by about 40%.

[53] In order to understand the basin-basin differences in the buoyancy term, the buoyancy frequency and MLD are separated from the buoyancy effect (B). Similarly, the logged and normalized factors are utilized to compare with each other as follows:

$$\begin{aligned}\langle b \rangle &\equiv \log(\mathrm{B}/\mathrm{B}^c) = 2\log(N/N^c) + 2\log(H_m/H_m^c) \\ &\equiv \langle N \rangle + \langle H_m \rangle,\end{aligned} \tag{15}$$

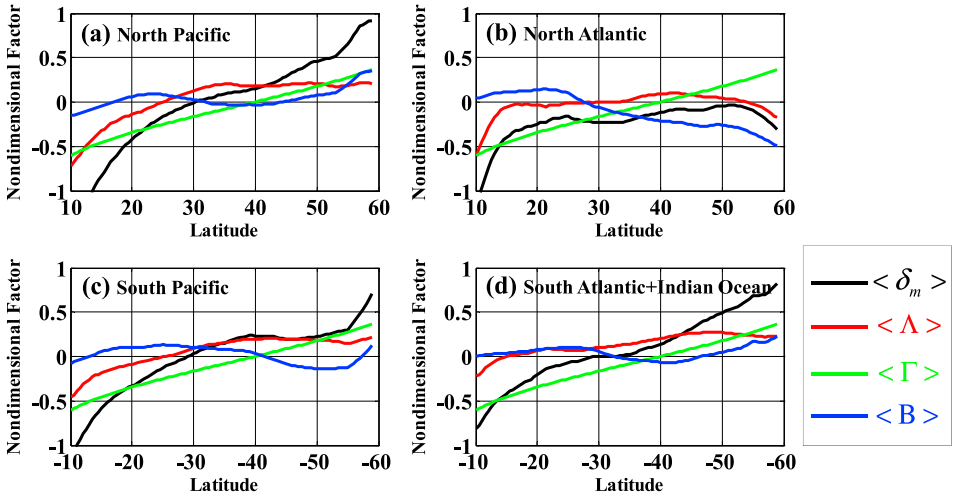

Figure 13. Contribution of each factor to the decay timescale for the (a) North Pacific, (b) North Atlantic, (c) South Pacific, and (d) South Atlantic and Indian Ocean. Black lines denote the logged and nondimensionalized decay time ($\langle\delta_{\mathrm{m}}\rangle$) obtained from the basin-averaged factors in the North Pacific. Similarly, forcing-scale effect (red, $\langle\Lambda\rangle$), Beta effect (green, $\langle\Gamma\rangle$), and buoyancy effect (blue, $\langle\mathrm{B}\rangle$). The detailed definitions are given in equation (14).

where B is defined by$N^2H_m^2$ as shown in (13) and the variables with superscript c denote the reference values obtained from the global average ($\mathrm{B}^c = 5.9\ m^2\ s^{-2}$; $N^c = 2.2 \times 10^{-2}\ s^{-1}$, and $H_m^c = 110\ m$). Figure 14 shows the spatial distributions of $\langle N\rangle$, $\langle H_m\rangle$, and $\langle b\rangle$. By comparing the buoyancy frequency and the MLD in each ocean basin, the spatial distribution of the buoyancy effect term can be understood. Larger buoyancy and MLD make decay timescales shorter. Spatial variability of the stratification term ($\langle b\rangle$) is smaller than that of the buoyancy frequency ($\langle N\rangle$) and the MLD ($\langle H_m\rangle$) by a factor of two, implying that the spatial variation of the buoyancy frequency is compensated for the MLD in terms of the stratification term. Let's look at the high latitude ($45 \sim 60°$) where only the large basin differences are exhibited, even though the North Pacific has a large buoyancy frequency which produces a rapid decay, its much shallower mixed layer makes the decay timescale longer. On the other hand, the MLD in the Southern Ocean is as deep as the North Atlantic, but the stratification below the mixed layer is weaker, compensating for the deep mixed layer. Thus, the decay timescale is longer than in the North Atlantic. The MLD in the North Atlantic is deep, but the buoyancy frequency is not small. Therefore, in the model results, buoyancy is responsible for the shortest decay timescale in the global ocean being found in the North Atlantic.

6. Discussion and Conclusions

[54] The temporal evolution of inertial motions is investigated by fitting satellite drifter trajectories over about a day to an inertial loop following *Park et al.* [2004]. The method enables us to obtain independent samples consecutively in time and to resolve the temporal evolution of inertial amplitudes. In this study, the decay timescales of inertial motion have been estimated by using temporal correlation functions of inertial amplitudes, providing the first estimates of the global distribution of the inertial decay timescale.

[55] Temporal correlation functions estimated from the drifter trajectory data are very close to exponential (Figure 6). Moreover, the theoretical model solution with beta dispersion also shows a decay pattern of inertial amplitudes similar to an exponential shape when the initial wave number is large enough (in section 4.1).

[56] E-folding timescales have meridional and basin-wide variations, consistent with the model (Figure 8). According to the linear model, the spatial distribution of the inertial decay timescale results mainly from the downward propagation of inertial-internal waves controlled by environmental factors such as β, f_o, H_m, and N_o. Since the initial wave in the model has a wavelength but its amplitude is spatially uniform, downward energy propagation is the only way to decay the mixed layer energy. Physically, the vertical group velocity of inertial waves can be expressed as

$$C_{g_z} = -\frac{N^2(k^2 + l^2)}{f_o m^3}, \tag{16}$$

where (k, l) is the horizontal wave number and m the vertical wave number [*Kunze*, 1985] in the absence of shear in the background flow. From (16), the group velocity increases in low latitudes due to small f_o so the decay timescale decreases. Likewise, a strong vertical density gradient (larger N_o) also makes the group velocity faster. *D'Asaro* [1989] and *Zervakis and Levine* [1995] pointed out that a gradient of planetary vorticity β makes an inertial wave refract by changing the meridional wave number l. The inertial wave number varies with βt like $|l| = |l_o - \beta t|$ (mostly inertial waves propagate equatorward; the direction of decreasing Coriolis frequency). Thus, large β also reduces the inertial decay timescale by increasing the group velocity. As for MLD, a larger MLD can provide a favorable environment to generate inertial-internal waves

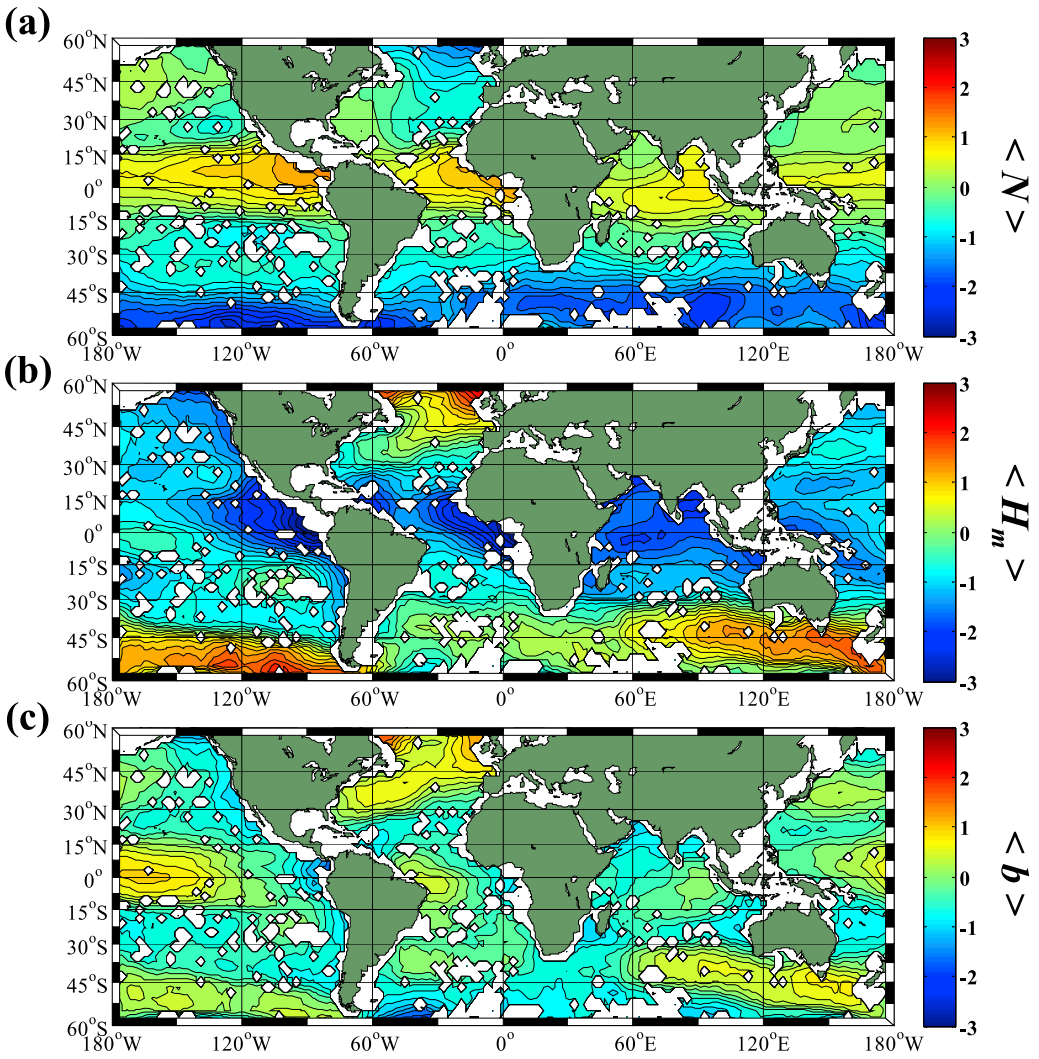

Figure 14. Decomposition of the (a) buoyancy frequency ($\langle N \rangle$), (b) mixed layer depth ($\langle H_m \rangle$), and (c) buoyancy factor ($\langle b \rangle$). Here $\langle b \rangle$ is equal to the summation of $\langle N \rangle$ and $\langle H_m \rangle$. The detailed definitions are given in equation (26).

of low vertical mode according to *Zervakis and Levine* [1995]. The combined effect of these factors through the physical processes mentioned above determines the decay rate of the mixed layer inertial motion in the model as shown in section 5.

[57] In this paper, it is assumed that the NIW initial meridional wave number l_0 should have negative sign which means most of NIWs are generated near the critical latitude (or the turning latitude) and propagate southward. Although this may be a reasonable assumption, if there is any northward propagating wave, it can stay longer at the base of the mixed layer. So, there is a possibility that the model results in this paper could underestimate the decay timescale. On the other hand, the initial zonal wave number is assumed to be zero in the model, but the wind forcing relevant to generating NIW has finite scales. This missing physics in the model would overestimate the decay timescale.

[58] The background flow field is the other factor which controls inertial-internal wave propagation but is not considered in the linear theoretical model. *Weller* [1982] proposed the possible effect of background flow divergence on the energy change in the mixed layer inertial motion. *Kunze* [1985] showed that the background shear flow modulates the local Coriolis frequency (approximately $f_{eff} = f_0 + \beta y + \zeta/2$) and traps the near-inertial wave in anticyclonic shear flow regions, where it can be dissipated [*Toole and Schmitt*, 1987; *Kunze et al.*, 1995]. This process could also change the spatial distribution of inertial energy. Additionally, *van Meurs* [1998] and *Klein et al.* [2004] pointed out that small-scale vorticity can play a role in the spatial heterogeneity of the surface inertial energy.

[59] Rectification effects on inertial wave numbers by spatial gradients in background shear flows may be one of the important factors responsible for the difference between the drifter observations and the model results. The western parts of North Pacific and North Atlantic have shorter decay timescales than the eastern part (not shown). The vorticity effect may be a plausible explanation for that, but it remains as a further study. In addition, *Balmforth and Young* [1999] suggested that a relative vorticity gradient may have a stronger effect on the high vertical modes. Since the modal spectrum is determined by the buoyancy structure [*Eriksen*, 1988; *Zervakis and Levine*, 1995] and by wave age (NIW energy of lower vertical mode rapidly escapes the mixed

layer but higher mode stays longer since formation), the decay of NIWs in the mixed layer may be strongly affected by the background shear field under a particular buoyancy environment, such as shallow mixed layers where the contribution of higher modes becomes important.

[60] Finally we note that greater detail in the seasonal variations in the decay timescale of inertial waves would be of interest, since there are strong seasonal changes in upper ocean stratification. Only a 6 month division between summer and winter was done here because of data limitations. This topic will be best investigated when a longer time period of drifter observations is available for the analysis or when another method to estimate temporal variation of the decay timescale is developed. Similarly, our spatial analysis is limited to zonal averages in each basin. Longer drifter track data sets will enable finer resolution in decay times scale estimates using this method in the future.

Appendix A

[61] This appendix presents mathematical descriptions of spatial and temporal correlation models for this analysis, which can give us insight into the physical meaning of e-folding scales from the correlation models.

A1. Temporal Correlation Function

[62] A temporal correlation function ($\gamma(\delta_k)$) at a time lag (δ_k) is

$$\gamma(\delta_k) = \frac{1}{\sigma^I \sigma^J} \sum_{(i,j)=1}^{N^l} (U_i - \overline{U}^I)(U_j - \overline{U}^J), (\delta_k = t_j - t_i, \quad i \neq j), \tag{A1}$$

where (U_i, U_j) are inertial amplitudes in each pair, (σ^I, σ^J) standard deviations of inertial amplitudes, ($\overline{U}^I$, $\overline{U}^J$) ensemble averages of all inertial amplitude data of the pairs with the time lag (δ_k), and N^l the number of the pairs, usually, $O(10^3) \sim O(10^4)$.

[63] An exponential fit is used to define the timescale from the correlation function. Assuming that the inertial motion exponentially decays in time, we can formulate it as follows:

$$U(t) = A \exp\left[-\left(\frac{t}{\lambda^t}\right)\right] + e, \tag{A2}$$

where A is an initial amplitude, λ^t decay timescale, and e random error. When the inertial amplitudes and their pairs are assumed to be sampled randomly; U_i, U_j ($i, j = 1, \ldots, N_k$) with some error (e_i, e_j), the covariance function

$$\begin{aligned}
\chi(\delta_k) &= \frac{1}{N_k} \sum_{(i,j)_k}^{N_k} (U_i - \overline{U}_k)(U_j - \overline{U}_k) \\
&= \frac{1}{N_k} \sum_{(i,j)_k}^{N_k} \left(A^2 \exp\left(-\frac{t_i + t_j}{2\lambda^t}\right) - U_i \overline{U}_k - U_j \overline{U}_k + \overline{U}_k^2 \right) \\
&\quad - \mathrm{cov}(e_i, U_j) - \mathrm{cov}(e_j, U_i) + \mathrm{cov}(e_i, e_j) \\
&\approx \exp\left(-\frac{\delta_k}{\lambda}\right) \left\{ \frac{1}{N_k} \sum_{(i,j)_k}^{N_k} \left(A^2 \exp\left(-\frac{2(t_i - \delta_k)}{\lambda^t}\right)\right)\right\} \\
&\quad - \overline{U}^2 + c,
\end{aligned} \tag{A3}$$

where a time separation $\delta_k = t_i - t_j$. The term in {} of (A3) becomes similar to the variance of U_i and U_j ($\sigma(U_i) \approx \sigma(U_j)$) when the time domain for subsampling is much larger than the time separation. Therefore, the correlation function, $\gamma(\delta_k) = \dfrac{\chi(\delta_k)}{\sigma(U_i)\sigma(U_j)} = \dfrac{\chi(\delta_k)}{\sigma^2}$ has an exponential

$$\chi(\delta_k) \approx \exp\left(-\frac{\delta_k}{\lambda}\right)\sigma^2(U) - \overline{U}^2 + c \tag{A4a}$$

$$\therefore \gamma(\delta_k) \approx \exp\left(-\frac{\delta_k}{\lambda}\right) + C, \tag{A4b}$$

where C is $(c - \overline{U}^2)/\sigma^2$.

A2. Spatial Correlation Function

[64] Introducing a simple function as in the previous section to estimate the spatial correlation scale, we assume that a spatial correlation function has a Gaussian spatial shape

$$U(x) = A \exp\left[-\left(\frac{x^2}{2\lambda^{s2}}\right)\right] + e, \tag{A5}$$

where the λ^s is the spatial scale defined as e-folding scale of the Gaussian function. The random sampling of U_i and U_j gives the correlation function

$$\begin{aligned}
\chi^s(\delta_k^s) &= \frac{1}{N_k} \sum_{(i,j)_k}^{N_k} (U_i - \overline{U}_k)(U_j - \overline{U}_k) \\
&= \frac{1}{N_k} \sum_{(i,j)_k}^{N_k} \left(A^2 \exp\left(-\frac{x_i^2 + x_j^2}{2\lambda^{s2}}\right) - U_i \overline{U}_k - U_j \overline{U}_k + \overline{U}_k^2 \right) \\
&\quad - \mathrm{cov}(e_i, U_j) - \mathrm{cov}(e_j, U_i) + \mathrm{cov}(e_i, e_j) \\
&\approx \frac{1}{N_k} \sum_{(i,j)_k}^{N_k} \left(A^2 \exp\left(-\frac{\left(x_i - \frac{\delta_k^s}{2}\right)^2 + \frac{\delta_k^{s2}}{4}}{2\lambda^{s2}} \right)\right) - \overline{U}^2 + c \\
&= \exp\left(-\frac{\delta_k^{s2}}{4\lambda^{s2}}\right) \left\{ \frac{1}{N_k} \sum_{(i,j)_k}^{N_k} \left(A^2 \exp\left(-\frac{2\left(x_i - \frac{\delta_k^s}{2}\right)^2}{2\lambda^{s2}} \right)\right)\right\} \\
&\quad - \overline{U}^2 + c
\end{aligned} \tag{A6a}$$

and then

$$\begin{aligned}
\chi^s(\delta_k) \approx \exp\left(-\frac{\delta_k^{s2}}{4\lambda^{s2}}\right) \mathrm{cov} \Bigg\{ & A \exp\left(-\frac{\left(x_i - \frac{\delta_k^s}{2}\right)^2}{2\lambda^{s2}} \right), \\
& A \exp\left(-\frac{\left(x_i - \frac{\delta_k^s}{2}\right)^2}{2\lambda^{s2}} \right) \Bigg\} - \overline{U}^2.
\end{aligned} \tag{A6b}$$

Under the assumption that the subsampling domain is much larger than the actual scale of inertial amplitude, the correlation function can be expressed

$$\therefore \gamma^s(\delta_k^s) \approx \exp\left(-\left(\frac{\delta_k^s}{2\lambda^s}\right)^2\right) + C, \tag{A7}$$

where C is $(c - \overline{U}^2)/\sigma^2$. Therefore, the e-folding scale of the spatial correlation is 2 times larger than the actual spatial scale under the assumption of Gaussian structure.

Appendix B

[65] This appendix shows algebra to get the solution of inertial amplitude in the mixed layer. Most of mathematical derivations are similar to *Moehlis and Smith* [2001], except the initial condition. From (8), taking the expansion of $A = A_0 + \varepsilon A_1 + O(\varepsilon^2)$ for the mixed layer ($0 < z < 1$), the leading order form of (8) at the base of the mixed layer is

$$A_{1zzt} + \frac{i}{2}A_{0yy} + iy\,A_{1zz} = 0. \tag{B1}$$

[66] Integrating (B1) subject to the boundary condition that A_{1z} becomes zero at $z = 1$ gives

$$A_{1zt} - \frac{i}{2}A_{0yy} + iyA_{1z} = 0 \qquad z = 0^+. \tag{B2}$$

Using $A_{yy} = A_{0yy} + O(\varepsilon)$, $A_z = \varepsilon A_{1z} + O(\varepsilon^2)$, $A_z|_{z=0^+} = \varepsilon A_z|_{z=0^-}$, and $A_{yy}|_{z=0^+} = A_{yy}|_{z=0^-}$.

[67] We can get the upper boundary condition of A in the ocean interior to leading order

$$A_{zt} - \frac{i}{2}A_{yy} + iyA_z = 0 \qquad z = 0^-. \tag{B3}$$

Thus, the governing equation for the interior becomes

$$A_{zzt} + \frac{i}{2}A_{yy} + iyA_{zz} = 0 \qquad z < 0, \tag{B4a}$$

$$A_{zt} - \frac{i}{2}A_{yy} + iyA_z = 0 \qquad z = 0^-, \tag{B4b}$$

$$A_z = -e^{-il_o y} \qquad t = 0, \tag{B4c}$$

$$A_{zz} \to 0 \qquad z \to \infty. \tag{B4d}$$

Taking $A(y, z, t) \equiv e^{-iy(t+l_o)}D(z, T)$, where $T = \frac{1}{3}\{(t+l_o)^3 - l_o^3\}$, the equations become

$$D_{zzT} - \frac{i}{2}D = 0 \qquad z < 0, \tag{B5a}$$

$$D_{zT} - \frac{i}{2}D = 0 \qquad z = 0^-, \tag{B5b}$$

$$D_z = -1 \qquad t = 0, \tag{B5c}$$

$$D_{zz} \to 0 \qquad z \to \infty. \tag{B5d}$$

[68] Defining the Laplace transform of $D(z, T)$ by $d(z, p) = \int_0^\infty D(z, T)e^{-pT}\,dT$, (11) can be transformed to

$$pd_{zz} - \frac{i}{2}d = D_{zz}|_{T=0} = 0 \qquad z < 0, \tag{B6a}$$

because T is zero at t = 0 and $A_{zz} = 0$ for $z < 0$ from (4). The boundary conditions become

$$pd_z + \frac{i}{2}d = D_z|_{T=0} = -1 \qquad z = 0^- \tag{B6b}$$

$$d_{zz} \to 0 \qquad z \to -\infty. \tag{B6c}$$

Thus, the solution is

$$d(z,p) = -\frac{1}{\sigma}\frac{1}{\sqrt{p}+\sigma}e^{(\sigma z/\sqrt{p})}, \tag{B7}$$

where $\sigma \equiv (1 + i)/2$.

[69] The amplitude evolution of the mixed layer inertial wave (α_m) can be expressed as $\alpha_m = |\frac{A^*_{zz}}{N^{*2}}| = |\mathrm{A}^*_{1zz}|$. By expanding $D(z, T) = D_0(z, T) + \varepsilon D_1(z, T) + O(\varepsilon^2)$, the equation (B1) becomes

$$D_{1zzT} - \frac{i}{2}D_0 = 0 \tag{B8}$$

and the Laplace transformed equation of (B8) is

$$pd_{1zz} - \frac{i}{2}d_0 = D_{1zz}(z, 0) = 1. \tag{B9}$$

[70] Since T = 0 at t = 0 and $A_{1zz}|_{t=0} = e^{-il_o y}$, the initial condition within the mixed layer is $D_{1zz}(z, 0) = 1$. Since D_0 is same as D_0(z = 0, T) within the mixed layer

$$d_{1zz} = \frac{1}{p} - \frac{i}{2\sigma p}\frac{1}{\sqrt{p}+\sigma}, \tag{B10}$$

using $d_0 = d(0^-, p) = -\frac{1}{\sigma}\frac{1}{\sqrt{p}+\sigma}$ for $0 < z < 1$ from (B7).

[71] By inverting (B10), we can obtain the second derivative of the complex field (A) that corresponds to the inertial oscillation field as follows:

$$A_{1zz}(y, t) = e^{-iy(t+l_0)}e^{i\tau^3/3}erfc\left(\frac{1+i}{2\sqrt{3}}\tau^{3/2}\right), \tag{B11}$$

where the complementary error function (*erfc*) is defined by $erfc(x) \equiv \frac{2}{\sqrt{\pi}}\int_x^\infty e^{-t^2}\,dt$ and $\tau = ((t + l_o)^3 - l_o^3)^{1/3}$.

[72] **Acknowledgments.** We are grateful for useful discussions and valuable comment from Stefan Llewellyn Smith of the University of California, San Diego. We thank Rick Lumpkin of NOAA for kindly helping to secure the satellite tracked drifter data. The drifter trajectory data are provided from the Drifter Data Assembly Center at AOML. Argo float data were collected and made freely available by the International Argo Project and the national programs that contribute to it (www.argo.ucsd.edu, argo.jcommops.org). Argo is a pilot program of the Global Ocean Observing System. Jong Jin Park was supported by a WHOI postdoctoral

scholarship. Ray Schmitt acknowledges NSF grant OCE 84794900. This study was partly supported by "A Study on the Monitoring of the Global Ocean Variability with ARGO Program" in Meteorological Research Institute/KMA. We also thank two anonymous reviewers for their thoughtful comments and constructive suggestions.

References

Balmforth, N. J., and W. R. Young (1999), Radiative damping of near-inertial oscillations in the mixed layer, *J. Mar. Res.*, *57*, 561–584, doi:10.1357/002224099321549594.

Chin, T. M., R. F. Milliff, and W. G. Large (1998), Basin-scale high-wavenumber sea surface wind fields from multiresolution analysis of scatterometer data, *J. Atmos. Oceanic Technol.*, *15*, 741–763, doi:10.1175/1520-0426(1998)015<0741:BSHWSS>2.0.CO;2.

D'Asaro, E. A. (1985), The energy flux from the wind to near-inertial motions in the mixed layer, *J. Phys. Oceanogr.*, *15*, 943–959, doi:10.1175/1520-0485(1985)015<0943:UOTSIC>2.0.CO;2.

D'Asaro, E. A. (1989), The decay of wind-forced mixed layer inertial oscillations due to the beta effect, *J. Geophys. Res.*, *94*, 2045–2056, doi:10.1029/JC094iC02p02045.

D'Asaro, E. A. (1995a), Upper ocean inertial currents forced by a strong storm. Part II: Modeling, *J. Phys. Oceanogr.*, *25*, 2937–2952, doi:10.1175/1520-0485(1995)025<2937:UOICFB>2.0.CO;2.

D'Asaro, E. A. (1995b), Upper ocean inertial currents forced by a strong storm. Part III: Interaction of inertial currents and mesoscale eddies, *J. Phys. Oceanogr.*, *25*, 2953–2958.

D'Asaro, E. A., C. C. Eriksen, M. D. Levine, P. Niiler, C. A. Paulson, and P. V. Meurs (1995), Upper-ocean inertial currents forced by a strong storm. Part I: Data and comparisons with linear theory, *J. Phys. Oceanogr.*, *25*, 2909–2936.

Efron, B., and G. Gong (1983), A leisurely look at the bootstrap, the jackknife, and cross validation, *Am. Stat.*, *37*(1), 36–48, doi:10.2307/2685844.

Eriksen, C. C. (1980), Evidence for a continuous spectrum of equatorial waves in the Indian Ocean, *J. Geophys. Res.*, *85*(C6), 3285–3303, doi:10.1029/JC085iC06p03285.

Eriksen, C. C. (1988), On wind forcing and observed oceanic wave number spectra, *J. Geophys. Res.*, *93*(C5), 4985–4992, doi:10.1029/JC093iC05p04985.

Eriksen, C. C. (1991), Observations of near-inertial internal waves and mixing in the seasonal theromocline, in *Dynamics of Oceanic Internal Gravity Waves: Proceedings of the 6th 'Aha Huliko'a Hawaiian Winter Workshop, 1991*, pp. 71–88, Univ. of Hawaii at Manoa, Manoa, Hawaii.

Freeland, H. J., P. B. Rhines, and H. T. Rossby (1975), Statistical observations of the trajectories of neutrally buoyant floats in the North Atlantic, *J. Mar. Res.*, *33*(3), 383–404.

Furuichi, N., T. Hibiya, and Y. Niwa (2008), Model-predicted distribution of wind-induced internal wave energy in the world's oceans, *J. Geophys. Res.*, *113*, C09034, doi:10.1029/2008JC004768.

Garrett, C. (2001), What is the "near-inertial" band and why is it different from the rest of the internal wave spectrum?, *J. Phys. Oceanogr.*, *31*, 962–971, doi:10.1175/1520-0485(2001)031<0962:WITNIB>2.0.CO;2.

Gill, A. E. (1984), On the behavior of inertial waves in the wakes of storms, *J. Phys. Oceanogr.*, *14*, 1129–1151, doi:10.1175/1520-0485(1984)014<1129:OTBOIW>2.0.CO;2.

Hansen, D. V., and P. M. Poulain (1996), Processing of WOCE/TOGA drifter data, *J. Atmos. Oceanic Technol.*, *13*, 900–909, doi:10.1175/1520-0426(1996)013<0900:QCAIOW>2.0.CO;2.

Hebert, D., and J. N. Moum (1994), Decay of a near-inertial wave, *J. Phys. Oceanogr.*, *24*, 2334–2351, doi:10.1175/1520-0485(1994)024<2334:DOANIW>2.0.CO;2.

Henyey, F. S., J. A. Wright, and S. M. Flatte (1986), Energy and action flow through the internal wave field: An eikonal approach, *J. Geophys. Res.*, *91*, 8487–8495, doi:10.1029/JC091iC07p08487.

Hisaki, Y., and T. Naruke (2003), Horizontal variability of near-inertial oscillations associated with the passage of a typhoon, *J. Geophys. Res.*, *108*(C12), 3382, doi:10.1029/2002JC001683.

Kara, A., P. Rochford, and H. Hurlburt (2000), An optimal definition for ocean mixed layer depth, *J. Geophys. Res.*, *105*(C7), 16,803–16,821, doi:10.1029/2000JC900072.

Klein, P., S. L. Smith, and G. Lapeyre (2004), Organization of near-inertial energy by an eddy field, *Q. J. R. Meteorol. Soc.*, *130*, 1153–1166.

Kunze, E. (1985), Near-inertial wave propagation in geostrophic shear, *J. Phys. Oceanogr.*, *15*, 544–565, doi:10.1175/1520-0485(1985)015<0544:NIWPIG>2.0.CO;2.

Kunze, E., R. W. Schmitt, and J. M. Toole (1995), The energy balance in a warm-core ring's near-inertial critical layer, *J. Phys. Oceanogr.*, *25*(5), 942–957, doi:10.1175/1520-0485(1995)025<0942:TEBIAW>2.0.CO;2.

Levine, M. D., and V. Zervakis (1995), Near-inertial wave propagation into the pycnocline during ocean storms: Observations and model comparison, *J. Phys. Oceanogr.*, *25*, 2890–2908, doi:10.1175/1520-0485(1995)025<2890:NIWPIT>2.0.CO;2.

MacKinnon, J. A., and K. B. Winters (2005), Subtropical catastrophe: Significant loss of low-mode tidal energy at 28.9°, *Geophys. Res. Lett.*, *32*, L15605, doi:10.1029/2005GL023376.

Moehlis, J., and S. G. L. Smith (2001), Radiation of mixed layer near-inertial oscillations in to the ocean interior, *J. Phys. Oceanogr.*, *31*, 1550–1560, doi:10.1175/1520-0485(2001)031<1550:ROMLNI>2.0.CO;2.

Nagasawa, M., Y. Niwa, and T. Hibiya (2000), Spatial and temporal distribution of the wind-induced internal wave energy available for deep water mixing in the North Pacific, *J. Geophys. Res.*, *105*, 13,933–13,943, doi:10.1029/2000JC900019.

Park, J. J., K. Kim, and W. R. Crawford (2004), Inertial currents estimated from surface trajectories of Argo floats, *Geophys. Res. Lett.*, *31*, L13307, doi:10.1029/2004GL020191.

Park, J. J., K. Kim, and B. A. King (2005), Global statistics of inertial motions, *Geophys. Res. Lett.*, *32*, L14612, doi:10.1029/2005GL023258.

Plueddemann, A., and J. Farrar (2006), Observations and models of the energy flux from the wind to mixed-layer inertial currents, *Deep Sea Res. Part II*, *53*, 5–30, doi:10.1016/j.dsr2.2005.10.017.

Pollard, R. T., and R. C. Millard (1970), Comparison between observed and simulated wind-generated inertial oscillations, *Deep Sea Res.*, *17*, 813–821.

Price, J. F. (1983), Internal wave wake of a moving storm. Part I: Scales, energy budget and observations, *J. Phys. Oceanogr.*, *13*, 949–965, doi:10.1175/1520-0485(1983)013<0949:IWWOAM>2.0.CO;2.

Shay, L. K., and R. L. Elsberry (1987), Near-inertial ocean current response to hurricane Frederic, *J. Phys. Oceanogr.*, *17*, 1249–1269.

Toole, J. M., and R. W. Schmitt (1987), Small-scale structures in the northwest Atlantic subtropical front, *Nature*, *327*(6117), 47–49, doi:10.1038/327047a0.

van Haren, (2007), Shear a the critical diurnal latitude, *Geophys. Res. Lett.*, *34*, L06601, doi:10.1029/2006GL028716.

van Meurs, (1998), Interactions between near-inertial mixed layer currents and the mesoscale: The importance of spatial variabilities in the vorticity field, *J. Phys. Oceanogr.*, *28*, 1363–1388, doi:10.1175/1520-0485(1998)028<1363:IBNIML>2.0.CO;2.

Visher, S. S. (1925), Effects of tropical cyclones upon the weather of mid-latitudes, *Geogr. Rev.*, *15*, 106–114.

Weller, R. A. (1982), The relation of near-inertial motions observed in the mixed layer during the JASIN (1978) experiment to the local wind stress and to the quasi-geostrophic flow field, *J. Phys. Oceanogr.*, *12*, 1122–1136, doi:10.1175/1520-0485(1982)012<1122:TRONIM>2.0.CO;2.

Young, W. R., and M. Ben Jelloul (1997), Propagration of near-inertial oscillations through a geostrophic flow, *J. Mar. Res.*, *55*(4), 735–766, doi:10.1357/0022240973224283.

Zervakis, V., and M. D. Levine (1995), Near-inertial energy propagation from the mixed layer: Theoretical considerations, *J. Phys. Oceanogr.*, *25*, 2872–2890, doi:10.1175/1520-0485(1995)025<2872:NIEPFT>2.0.CO;2.

K. Kim, Ocean Science and Technology Institute, Pohang University of Science and Technology, San 31, Hyoja-Dong, Nam-Gu, Pohang 790-784, South Korea. (kuhkim@postech.ac.kr)

J. J. Park and R. W. Schmitt, Department of Physical Oceanography, Woods Hole Oceanographic Institution, MS 21, 266 Woods Hole Road, Woods Hole, MA 02543, USA. (jjpark@whoi.edu)